


Article

Trace of Chemical Reactions Accompanied with Arrhenius Energy on Ternary Hybridity Nanofluid Past a Wedge

Tanveer Sajid ¹, Assad Ayub ², Syed Zahir Hussain Shah ², Wasim Jamshed ^{1,*}, Mohamed R. Eid ^{3,4}, El Sayed M. Tag El Din ⁵, Rida Irfan ⁶ and Syed M. Hussain ⁷

¹ Department of Mathematics, Capital University of Science and Technology, Islamabad 44000, Pakistan

² Department of Mathematics & Statistics, Hazara University, Manshera 21300, Pakistan

³ Department of Mathematics, Faculty of Science, New Valley University, Al-Kharga 72511, Al-Wadi Al-Gadid, Egypt

⁴ Department of Mathematics, Faculty of Science, Northern Border University, Arar 1321, Saudi Arabia

⁵ Electrical Engineering, Faculty of Engineering and Technology, Future University in Egypt, New Cairo 11835, Egypt

⁶ Department of Mathematics, Sahiwal Campus, COMSATS University Islamabad, Islamabad 45550, Pakistan

⁷ Department of Mathematics, Faculty of Science, Islamic University of Madinah, Madinah 42351, Saudi Arabia

* Correspondence: wasiktk@hotmail.com

Highlights:

What are the main findings?

- The problem of 2-D Prandtl nanofluid past a moving wedge is investigated in detail;
- Tri-hybrid nanoparticles are considered here;
- Heat and mass transmission evaluations are conducted in the presence of endothermic/exothermic chemical reactions;
- The moving wedge is considered;

What is the implication of the main finding?

- LobattoIIIA scheme is implemented for the numerical solution of modeled PDEs.

Abstract: Heat transfer is a vital fact of daily life, engineering, and industrial mechanisms such as cryogenic systems, spaceborne thermal radiometers, electronic cooling, aircraft engine cooling, aircraft environmental control systems, etc. The addition of nanoparticles helps to stabilize the flowing of a nanofluid and keeps the symmetry of the flowing structure. **Purpose:** In this attempt, the effect of endothermic/exothermic chemical reactions accompanied by activation energy on a ternary hybrid nanofluid with the geometry of a wedge is taken into consideration. The mathematical form of PDEs is obtained by Navier–Stokes equations, the second law of thermodynamics, and Fick’s second law of diffusion. The geometric model is therefore described using a symmetry technique. **Formulation:** The MATLAB built-in Lobatto III A structure is utilized to find the computational solution of the dimensionless ODEs. All computational outcomes are presented by graphs and statistical graphs in order to check the performance of various dimensionless quantities against drag force factor and Nusselt quantity. **Finding:** the addition of tri-hybridizing nanomolecules in the standard liquid improves the thermic performance of the liquid much better in comparison to simple hybrid nanofluids. Wedge angle parameter α brings about a decrement in fluid velocity and augmentation in thermal conductivity ϵ , thermal radiation Rd , thermophoresis parameter Nt and endothermic/exothermic reaction Ω , and fitted rate constant n accelerates the heat transmission rate. **Novelty:** The effect of tri-hybridizing nanomolecules along with endothermic/exothermic reactions on the fluid past a wedge have not been investigated before in the available literature.

Keywords: tri-hybrid nanofluid; prandtl fluid; variable thermal conductivity; thermal radiation; activation energy; buongiorno model



Citation: Sajid, T.; Ayub, A.; Shah, S.Z.H.; Jamshed, W.; Eid, M.R.; El Din, E.S.M.T.; Irfan, R.; Hussain, S.M. Trace of Chemical Reactions Accompanied with Arrhenius Energy on Ternary Hybridity Nanofluid Past a Wedge. *Symmetry* **2022**, *14*, 1850. <https://doi.org/10.3390/sym14091850>

Academic Editor: Ghulam Rasool

Received: 28 July 2022

Accepted: 22 August 2022

Published: 5 September 2022

Publisher’s Note: MDPI stays neutral with regard to jurisdictional claims in published maps and institutional affiliations.



Copyright: © 2022 by the authors. Licensee MDPI, Basel, Switzerland. This article is an open access article distributed under the terms and conditions of the Creative Commons Attribution (CC BY) license (<https://creativecommons.org/licenses/by/4.0/>).

1. Introduction

Mixing nanoparticles with a base fluid, such as water, oil, etc., to promote the thermal characteristics of fluid is called a hybrid nanofluid. Hybrid materials can combine the physical and chemical properties of various substances. Base material and its characteristics are encouraged by hybrid nanofluid because it unites the thermophysical characteristics of others. A single material cannot possess desirable properties for the required thermal system; due to this factor, many scholars [1,2] analyzed hybrid fluids and their applications in the era of the science of technology. The flow, heat, and mass transfer from a flat plate with a specified surface heat flux have been studied using the Buongiorno model to determine how Brownian motion and thermophoresis affect these processes. To anticipate the characteristics of heat transmission, a newly created model known as the modified Buongiorno model is used, which examines the effects of the thermophoretic phenomena and the Brownian diffusion phenomenon. Research across the world has tried to explore the impact of thermophoresis and the Brownian motion effect, along with the volume fractional of nanoparticles, on hybrid nanofluids movement subjected to various flow geometries such as a cone, wedge, sheet, channels, etc. Owhaib et al. [3] investigated the impact of a modified Buongiorno nanofluid model to investigate the impact of heat flux and dissipation heat on hybrid nanofluid past a sheet. Rosca et al. [4] investigated the impact of zero mass flux and slip boundary conditions on fluid using a modified Buongiorno nanofluid model past an expandable/shrinkable sheet. Rana and Gupta [5] achieved the numerical solution of a three-dimensional fluid past a wedge using a modified Buongiorno nanofluid model. Mousavi et al. [6] discussed particle volume concentration and related effects of temperature with attached rheology performance of CuO/MgO/TiO₂ aquatic ternary hybridizing nanoliquid. The latest study regarding the development of practical correlations and viscosity and thermal conducting of H₂O-Cu-SiO₂-MWCNT attaching the mathematical model of ternary hybrid nanofluid by Dezfulizade et al. [7].

Non-Newtonian fluids have various applications in daily life such as toothpaste, shampoo, honey, paints, cosmetics, greases, etc. Due to the non-linear relation between shear stress and strain it is difficult to predict the exact nature of the fluid flow. Various mathematical fluid models such as Maxwell, Casson, viscoelastic, couple stress, Prandtl fluid models, and power-law fluid models such as Carreau fluid, Cross fluids, and other models have been defined to see the nonlinear relationship of the non-Newtonian fluids. Prandtl fluid is also known as Prandtl–Eyring fluid, which minutely investigates the physical aspect of visco-inelastic fluids. This model comprises a relationship of a linear nature between sine hyperbolic function and shear stress. Researchers across the world have tried to investigate the impact of Prandtl–Eyring fluid flow over various geometries. Munjam et al. [8] employed a novel MDDIM technique to achieve the numerical solution of magneto radiative Prandtl fluid moving subjected to an expandable surface. The effects of activation energy and melting boundary conditions on Prandtl liquid were deeply investigated by Ullah et al. [9]. Qureshi [10] scrutinized the impact of hybrid nanoparticles and MHD on Prandtl fluid flow towards a slippery surface. Figure 1a is designed to display the application of nanofluid in various daily life use products.

The natural transformation of two or more materials into an additional two materials is called chemically reactive flow. Daily life involves chemical processes such as tea-making, photosynthesis, washing with soap and water, chemical batteries, digestion, sweltering of papers and logs of wood, boiling an egg, absorption of food, baking a cake, chemically battery use, milk turning sour and different biochemical processes that occur in tissues. Chemical processes also keep their influence in fluid dynamics and have key applications [11–20]. Ellahi et al. [21] made the analysis of peristaltic blood flow suspended with nanoparticles with facts of activation energy and chemical process. Khan et al. [22] did their investigation related to chemical reaction and variable reactive index on third-grade magneto liquid flowing underneath the impact of heat transport. The relation between activation energy, chemical reaction, and viscous dissipation over electrically conducting Casson liquid is discussed by Vijaya et al. [23]. Ali et al. [24] conducted a numerical analysis

taking the model of Oldroyd-B liquid dynamic along the geometry of the upper horizontal plate. Zaib et al. [25] investigated the impact of nanoparticles and mixed convection on micropolar Prandtl fluid moving over a wedge. Habib et al. [26] utilized the Keller box method to numerically achieved the solution of magnetically driven Prandtl fluid moving towards an expandable wedge and discussed the radiation effect and chemical reaction by considering the porous medium along with a mathematical model of MHD Casson fluid.

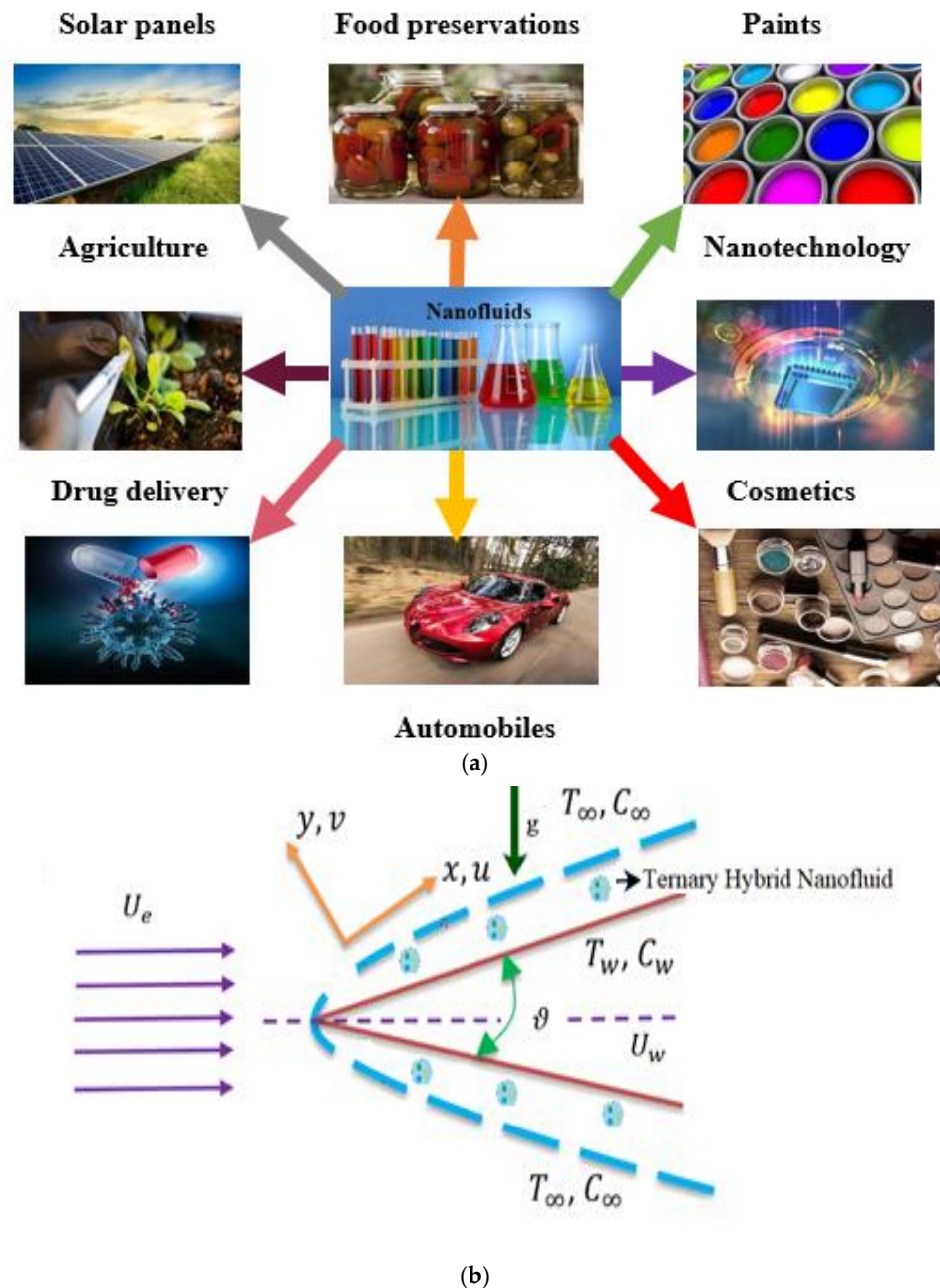


Figure 1. (a). Implementations of nanofluid. (b) Geometry of the fluid flow.

A minimum amount of energy that helps during the initiation of the chemical process is called activation energy. Activation energy is quite similar to the energy that is required to start the engine of a vehicle. Geothermal engineering, thermal oil recovery, nuclear reactors, chemical energy, food processing, and water emulsion are examples of activation energy. Activation energy is made by Shah et al. [27]. Bhatti and Michaelides [28] established the study of thermo-bioconvection nanofluid flow by considering the magnetized Riga plate with an attachment of Arrhenius activation energy. Other recent studies have been con-

ducted by several authors [29–31] such as on the heat and mass transmissions of Marangoni propelled boundary layer flowing, interpreting melting heat and the magnetized transient flowing of Prandtl–Eyring liquid, and unsteadiness nanoliquid slippage transportation results in the extendable region.

The utilization of Falkner–Skan flow is found in the areas of aerodynamics and hydrodynamics. From an application point of view, it seems to be fundamental for different fields such as atomic waste stockpiling, geothermal enterprises, and improved oil recuperation. Several scholars conducted their investigations by taking different mathematical models along with the wedge. Cross nanofluid with non-uniform heat sink source and Lorentz force was carried out by Asogwa et al. [32]. In this study, it was considered that fluid flows over the wedge and the numerical analysis was performed with wedge parameter r . The influence of an inclined magnetic field concerning the Carreau fluid model associated with a wedge was scrutinized by Ali et al. [33]. Recent works [34–36] on wedges have been published, such as on wedge penetrating fluid interfaces, porousness stretchable wedges in non-linear radiative fluxing, the suspension of nanoparticles across a wedge, and mass transfer along with transient subduction interfaces of the wedge.

Nanofluid past a wedge with the inclusion of various effects mentioned above has distinguished applications in the industrial and engineering sectors such as the processing of polymers, the extraction of crude oil in the oil field industry, flow in the case of molten metals, flows of the liquid metals in heat exchangers, submarines, warships design, designing flaps on airplane wings, and nuclear power plants. The effect of endothermic/exothermic chemical reactions accompanied by activation energy on ternary hybrid nanofluid with the geometry of wedges is considered. The mathematical form of PDEs is obtained by Navier–Stokes equations and further PDEs are converted into ODEs for numerical solution purposes. The shooting technique converts the BVP into IVP which makes it fit for applying MATLAB process bvp4c. All numerical outcomes are presented in graphs and statistical graphs.

2. Mathematical Formulation

The simulation of mixed convective Prandtl–Eyring fluid dispersed with tri hybrid nanoparticles with the consideration of ethylene glycol (E-G) as a standard liquid is shown in Figure 1b. The heat transmission event was studied with the addition of endothermic/exothermic reactions and activation energy whereas. The mass transfer analysis was studied in the light of the activation energy effect. The temperature variation was analyzed with the help of inconstant thermal conduction and radiation heat fluxing. Rosseland radiative heat fluxing was considered in the case of the heat transmission study. A modified Buongiorno nanofluid was considered, which is the combination of ternary hybrid nanofluid, Brownian diffusion, and thermophoresis effects. The parameters U_w and U_e depict the stretching velocity and ambient rapidity. The temperature, aside from concentration at the wall and the ambient temperature in addition to the concentration, is represented by T_w , C_w , T_∞ , C_∞ . Further, it is assumed that $T_w > T_\infty$ and $C_w > C_\infty$. The wedge is positioned along the x -axis with the y -axis vertical to it. The gravitational acceleration g is applied to the wedge direction and the wedge angle is mentioned by α . The parameters ρ_{thnf} , $(\rho C_p)_{thnf}$ and k_{thnf} represent density, specific heat, and thermal conduction of ternary hybrid nanoliquid, correspondingly. Under the effect of boundary layer assumption, the effects such as viscous dissipation and Joules' heating were neglected, and Boussinesq's approximation was considered because of the buoyancy-driven mixed convection effect adopted in the momentum equation. The continuity, momentum, energy, and concentration equations are derived with the utilization of the law of conservation of mass, Navier–Stokes equation, the second law of thermodynamics, and Fick's second law of diffusion.

The momentum is derived from Newton's second law of motion. The left-hand side of the momentum equation represents the combination of convective transport and material derivative whereas the right-hand side indicates the momentum diffusion phenomenon

comprised of Prandtl fluid, the stagnation point effect, and the buoyancy phenomenon. The temperature mentioned in Equation (3) is derived from the second law of thermodynamics. The left-hand side is the combination of convective term and local derivative and the right hand is the thermal diffusion phenomenon comprised of variable thermal conductivity, nanofluid terms, thermal radiation, and endothermic/exothermic reactions. In Equation (4), left-hand terms represent convective terms derived from Fick's first law whereas the right-hand side derives from Fick's second law of diffusion. The first two terms on the right side represent nanofluid concentration and temperature diffusion and the term after the negative sign represents activation energy. Based on the hypotheses, the equations for continuity, momentum, heat, and concentration [15,33,37] are mentioned underneath.

$$\frac{\partial u}{\partial x} + \frac{\partial v}{\partial y} = 0, \quad (1)$$

$$u \frac{\partial u}{\partial x} + v \frac{\partial u}{\partial y} = U_e \frac{dU_e}{dx} + \frac{\mu_{thnf}}{\rho_{thnf}} \left[\frac{L}{C_1} \frac{\partial^2 u}{\partial y^2} + \frac{L}{2C_1^3} \left(\frac{\partial u}{\partial y} \right)^2 \frac{\partial^2 u}{\partial y^2} \right] + \frac{1}{\rho_{thnf}} [g\beta(T - T_\infty) + g\beta^*(C - C_\infty)] \frac{\sin \alpha}{2}, \quad (2)$$

$$u \frac{\partial T}{\partial x} + v \frac{\partial T}{\partial y} = \frac{\partial}{\partial y} \left(\frac{k_{thnf}}{(\rho C_p)_{thnf}} \frac{\partial T}{\partial y} \right) + \tau \left[D_B \frac{\partial C}{\partial y} \frac{\partial T}{\partial y} + \frac{D_T}{T_\infty} \left(\frac{\partial T}{\partial y} \right)^2 \right] - \frac{1}{(\rho C_p)_{thnf}} \frac{\partial q_r}{\partial y} + \frac{1}{(\rho C_p)_{thnf}} \Omega K_r^2 (C - C_\infty) \left(\frac{T}{T_\infty} \right)^n \exp \left(\frac{-E_a}{\kappa T} \right), \quad (3)$$

$$u \frac{\partial C}{\partial x} + v \frac{\partial C}{\partial y} = D_B \left(\frac{\partial^2 C}{\partial y^2} \right) + \frac{D_T}{T_\infty} \left(\frac{\partial^2 T}{\partial y^2} \right) - K_r^2 (C - C_\infty) \left(\frac{T}{T_\infty} \right)^n \exp \left(\frac{-E_a}{\kappa T} \right). \quad (4)$$

The symbols U_e , L , C_1 , g , β , β^* , α , D_B , D_T , q_r , Ω , K_r , n , E_a , τ used in Equations (1)–(4) represent wedge velocity, Prandtl fluid parameter, elastic parameter, gravity, thermal expansion, concentration expansion, wedge angle, Brownian diffusion, thermophoretic diffusion, radiative heat flux, endothermic/exothermic reaction, the reaction rate constant, power law index, activation energy, the ratio of specific heat at constant pressure to volume.

The associated boundary conditions [34,37] are:

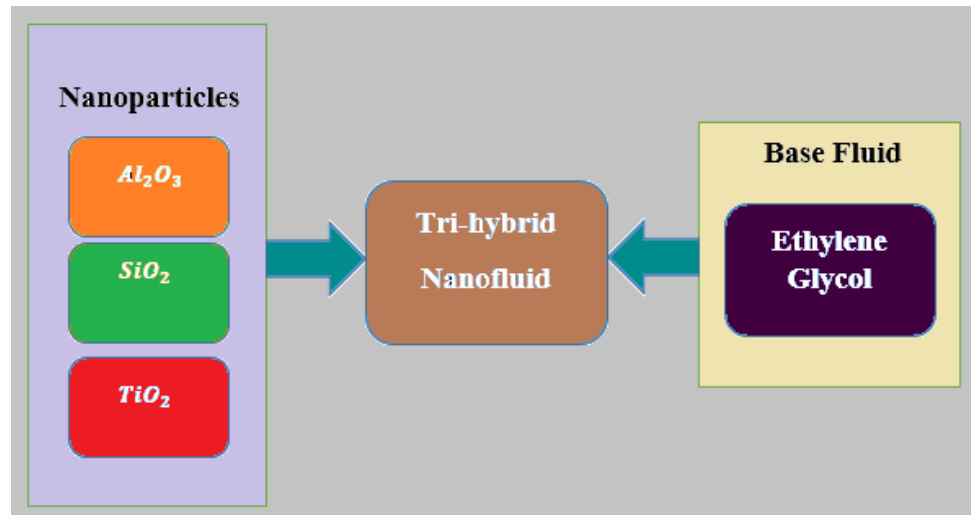
$$\left. \begin{aligned} y = 0 : u = U_w(x) = U_e, v = 0, T = T_w, C = C_w, \\ y \rightarrow \infty : u \rightarrow U_e, T = T_\infty, C = C_\infty. \end{aligned} \right\} \quad (5)$$

The following mathematical formulas for the thermal physical characteristics of ternary hybrid nanoliquid [9,10] are enumerated underneath.

$$\left. \begin{aligned} \mu_{Thnf} &= \frac{\mu_f}{(1 - \phi_1)^{2.5} (1 - \phi_2)^{2.5} (1 - \phi_3)^{2.5}}, \\ \rho_{Thnf} &= [(1 - \phi_1) \{ (1 - \phi_2) [(1 - \phi_3)\rho_f + \rho_3\phi_3] + \rho_2\phi_2 \} + \rho_1\phi_1], \\ (\rho C_p)_{Thnf} &= (1 - \phi_1) \{ (1 - \phi_2) [(1 - \phi_3)(\rho C_p)_f + (\rho C_p)_{s_3}\phi_3] + \\ &(\rho C_p)_{s_2}\phi_2 \} + (\rho C_p)_{s_1}\phi_1, \\ \frac{k_{Thnf}}{k_{hnf}} &= \frac{k_1 + 2k_{nf} - 2\phi_1(k_{nf} - k_1)}{k_1 + 2k_{nf} + \phi_1(k_{nf} - k_1)}, \\ \frac{k_{hnf}}{k_{nf}} &= \frac{k_2 + 2k_{nf} - 2\phi_2(k_{nf} - k_2)}{k_2 + 2k_{nf} + \phi_2(k_{nf} - k_2)}, \\ \frac{k_{nf}}{k_f} &= \frac{k_3 + 2k_{nf} - 2\phi_3(k_{nf} - k_3)}{k_3 + 2k_{nf} + \phi_3(k_{nf} - k_3)}. \end{aligned} \right\} \quad (6)$$

In Equation (6) Th reflects ternary hybrid, $Thnf$ represents ternary hybrid nanofluid, hnf is hybrid nanofluid, nf represents nanofluid, ρ_{Thnf} indicates the density of ternary

hybrid nanofluid, $(\rho C_p)_{Tnfnf}$ depicts specific heat of ternary hybrid nanofluid, $(\rho C_p)_{Tnfnf}$ indicates thermal conductivity of ternary hybrid nanofluid. The symbols ϕ_1, ϕ_2, ϕ_3 indicates volume fraction of tri, di, and mono hybrid nanoparticles. Figure 2a is planned to depict the total theme of ternary hybrid nanofluid. Ternary hybrid nanofluid is the combination of three different nanoparticles and E-G (Table 1) as the standard liquid. Figure 2b presents the comparison of thermophysical properties of bi and tri-hybridizing nanofluids.



(a)

Nanofluid

Ternary Hybrid Nanofluid

$$\mu_{Tnfnf} = \frac{\mu_f}{(1 - \phi_1)^{2.5}(1 - \phi_2)^{2.5}(1 - \phi_3)^{2.5}}$$

$$\rho_{Tnfnf} = [(1 - \phi_1)((1 - \phi_2)[(1 - \phi_3)\phi_f + \rho_3\phi_3] + \rho_2\phi_2] + \rho_1\phi_1$$

$$(\rho C_p)_{Tnfnf} = (1 - \phi_1)[(1 - \phi_2)[(1 - \phi_3)(\rho C_p)_f + (\rho C_p)_3\phi_3] + (\rho C_p)_2\phi_2 + (\rho C_p)_1\phi_1$$

$$\frac{k_{Tnfnf}}{k_{nf}} = \frac{k_1 + 2k_{nf} - 2\phi_1(k_{nf} - k_1)}{k_1 + 2k_{nf} + \phi_1(k_{nf} - k_1)}$$

$$\frac{k_{nf}}{k_f} = \frac{k_2 + 2k_{nf} - 2\phi_2(k_{nf} - k_2)}{k_2 + 2k_{nf} + \phi_2(k_{nf} - k_2)}$$

$$\frac{k_{nf}}{k_f} = \frac{k_3 + 2k_{nf} - 2\phi_3(k_{nf} - k_3)}{k_3 + 2k_{nf} + \phi_3(k_{nf} - k_3)}$$

Hybrid Nanofluid

$$\mu_{hnf} = \frac{\mu_f}{(1 - \phi_1)^{2.5}(1 - \phi_2)^{2.5}}$$

$$\rho_{hnf} = (1 - \phi_2)[(1 - \phi_1)\rho_f + \rho_1\phi_1] + \rho_2\phi_2$$

$$(\rho C_p)_{hnf} = (1 - \phi_2)[(1 - \phi_1)(\rho C_p)_f + (\rho C_p)_1\phi_1] + (\rho C_p)_2\phi_2$$

$$\frac{k_{hnf}}{k_{nf}} = \frac{k_2 + 2k_{nf} - 2\phi_2(k_{nf} - k_2)}{k_2 + 2k_{nf} + \phi_2(k_{nf} - k_2)}$$

$$\frac{k_{nf}}{k_f} = \frac{k_1 + 2k_f - 2\phi_1(k_f - k_1)}{k_1 + 2k_f + \phi_1(k_f - k_1)}$$

(b)

Figure 2. (a). Tri-hybrid nanofluid. (b). Comparison of hybrid and trihybrid nanofluids.

Table 1. Thermophysical properties.

Properties	Ethylene Glycol (EG)	Al_2O_3	TiO_2	SiO_2
ρ	1115	6310	4250	2270
C_p	4179	773	690	765
k	0.253	32.9	8.953	1.4013

The term for the Rosseland estimation [19] is:

$$q_r = -\frac{4\sigma^*}{3\kappa^*} \frac{\partial T^4}{\partial y}, \quad (7)$$

where σ^* and κ^* represent the Boltzmann parameter and the absorptivity, accordingly. The relevant conversions [33,37] listed below.

$$\left. \begin{aligned} \psi &= \left(\frac{2vxU_\infty x^m}{m+1} \right)^{\frac{1}{2}} f(\eta), \quad \eta = \left(\frac{U_\infty x^{m(m+1)}}{2vx} \right)^{\frac{1}{2}} y, \quad \theta(\eta) = \frac{T-T_\infty}{T_w-T_\infty}, \\ \phi(\eta) &= \frac{C-C_\infty}{C_w-C_\infty}. \end{aligned} \right\} \quad (8)$$

Equations (2)–(4) are converted as a result of the preceding conversions into the resulting dimensionless given by:

$$Af''' + Bf''^2 f''' + A_1 A_2 \frac{m+1}{2} f f'' + A_1 A_2 m (1 - f'^2) + A_1 \gamma_1 (\theta + N\phi) \frac{\sin \alpha}{2} = 0, \quad (9)$$

$$\left[\left((1 + \epsilon\theta) + \frac{Rd}{A_3} \right) \theta'' + \epsilon\theta'^2 \right] + \frac{A_3}{A_4} Pr f \theta' + \frac{A_3}{A_4} Pr (N_b \theta' \phi' + N_t \theta'^2) + \frac{1}{A_3} \Omega \beta_1 (1 + \delta\theta)^n \exp\left(\frac{-Q}{1 + \delta\theta}\right) \phi = 0, \quad (10)$$

$$\phi'' + \left(\frac{N_t}{N_b} \right) \theta'' + Sc f \phi' - \beta_1 Sc (1 + \delta\theta)^n \exp\left(\frac{-Q}{1 + \delta\theta}\right) \phi = 0, \quad (11)$$

The constraints (5) are written as follows:

$$\left. \begin{aligned} \eta = 0 : f(\eta) = 0, f'(\eta) = \lambda, \theta = 1, \phi = 1 \\ \eta \rightarrow \infty : f'(\eta) \rightarrow 1, \theta(\eta) \rightarrow 0, \phi(\eta) \rightarrow 0. \end{aligned} \right\} \quad (12)$$

The dimensionless parameters $A, B, m, \gamma_1, \alpha, \epsilon, Rd, Pr, N_b, N_t, \beta_1, \delta, Q, Sc, \lambda$ appears after numerical simulation of the problem in Equations (9)–(12) indicates Prandtl fluid parameter, elastic fluid parameter, dimensionless wedge parameter, buoyancy parameter, wedge angle, thermal conductivity, thermal radiation, Prandtl number, Brownian diffusion, thermophoresis parameter, the reaction rate constant, temperature difference parameter, activation energy, Schmidt number and the stagnation parameter.

3. Physical Quantities

The parameters like drag coefficient C_f , heat transmission rate Nu_x and mass transmission rate Sh_x are [34–37]:

$$C_f = \frac{2\tau_w}{\rho_f u_w^2}, \quad Nu_x = \frac{xq_w}{k_f(T_w - T_\infty)}, \quad \left. \right\} \quad (13)$$

whereas expressions regarding stress tensor τ_w , heat flux q_w , mass flux q_m are given below [25,26]:

$$\left. \begin{aligned} \tau_w &= \mu_{nf} \left[\frac{A}{C_1} \frac{\partial u}{\partial y} + \frac{A}{2C_1^3} \left(\frac{\partial u}{\partial y} \right)^3 \right], \\ q_w &= -k_{thnf} \left(\frac{\partial T}{\partial y} \right) + q_r. \end{aligned} \right\} \quad (14)$$

By substituting Equation (14) in Equation (13) and using the similarity transformation, the quantities defined in Equation (13) are non-dimensional as [25,26]:

$$\left. \begin{aligned} \frac{1}{2} C_f Re^{1/2} &= \frac{1}{A_1} [A f'' + B f''^3], \\ Nu_x Re_x^{-1/2} &= -(A_3 + Rd) \theta', \end{aligned} \right\} \quad (15)$$

where $Re_x = \frac{u_w x}{\nu}$. The following non-dimensional variables are derived from Equations (9)–(12):

$$\left. \begin{aligned} \lambda &= \frac{2m}{m+1}, A = LC_1, B = \left(\frac{L}{2C_1^3} \right) \left(\frac{U_\infty^3 x^{3m-1} (m+1)}{2\nu} \right), \\ Pr &= \frac{\mu C_p}{k_\infty}, R_d = \frac{16\sigma T_\infty^3}{3k^* k_\infty}, \gamma_1 = \frac{Grx}{Re_x^2}, Re_x = \frac{u_e(x)x}{\nu}, \\ Q &= \left(\frac{E_a}{\kappa T_\infty} \right), \delta = \frac{T_w - T_\infty}{T_\infty}, Nb = \frac{\tau D_B}{\nu} (C_w - C_\infty), \\ \beta_1 &= \sigma k_r^2, Nt = \frac{D_T \tau}{T_\infty \nu} (T_w - T_\infty), \tau = \frac{\rho C_p}{\rho C_f}, \\ Sc &= \frac{\nu}{D_B} \end{aligned} \right\} \quad (16)$$

where as A_1, A_2, A_3, A_4 indicates that viscosity, density, specific heat, and thermal conduction of ternary hybrid nanoparticles given by [9,10]:

$$\left. \begin{aligned} A_1 &= \frac{1}{(1-\phi_1)^{2.5} (1-\phi_2)^{2.5} (1-\phi_3)^{2.5}}, \\ A_2 &= (1-\phi_1) \left\{ (1-\phi_2) \left[(1-\phi_3) + \phi_3 \frac{\rho_3}{\rho_f} \right] + \phi_2 \frac{\rho_2}{\rho_f} \right\} + \phi_1 \frac{\rho_1}{\rho_f}, \\ A_3 &= (1-\phi_1) \left\{ (1-\phi_2) \left[(1-\phi_3) + \frac{(\rho C_p)_{s_3}}{(\rho C_p)_f} \phi_3 \right] + \frac{(\rho C_p)_{s_2}}{(\rho C_p)_f} \phi_2 \right\} + \frac{(\rho C_p)_{s_1}}{(\rho C_p)_f} \phi_1, \\ A_4 &= \frac{k_{hmf}}{k_f} \end{aligned} \right\} \quad (17)$$

4. Solution Methodology

The above nonlinear ODEs (9–11) accompanied by boundary constraints (12) can be handled numerically with the deployment of the Lobatto IIIA scheme incorporated with the `bvp4c` MATLAB built-in routine. The detailed flow chart procedure of Lobatto IIIA is mentioned below. The first step is all about the problem formulation comprising various effects incorporated in momentum, temperature, and concentration equations. The demonstrated PDEs are rehabilitated into ODEs with the assistance of suitable transformations in the second step. The nonlinear higher-order ODEs are altered into first-order ODEs in the light of the Lobatto IIIA scheme mentioned in step three, while the last step in the block diagram represents the effect of diverse dimensionless factors on the rapidity and temperature and concentration outlines. The tolerance level in the case of the present problem is 10^{-6} . The nonlinear ODEs are converted into first-order ODEs with the utilization of Lobatto IIIA by considering $f = w_1, f' = w_2, f'' = w_3, \theta = w_4$ and $\phi = w_6$, the resulting system of first-order ODEs are:

$$f = w_1, \quad (18)$$

$$f' = w_2, \quad (19)$$

$$f'' = w_3, \quad (20)$$

$$f''' = \frac{-\left(A_1 A_2 \frac{m+1}{2} w_1 w_3 + A_1 A_2 m (w_2^2 - 1) + A_1 \gamma_1 (w_4 + N w_6) \frac{\sin \alpha}{2} \right)}{A + B w_3^2}, \quad (21)$$

$$\theta' = w_5, \quad (22)$$

$$\theta'' = \frac{-\left(\epsilon w_5^2 + \frac{A_3}{A_4} Pr w_1 w_5 + \frac{A_3}{A_4} Pr (N_b w_5 w_7 + N_t w_5^2) + \frac{1}{A_3} \Lambda \beta_1 (1 + \delta w_4)^n \exp\left(\frac{-E}{1 + \delta w_4}\right) w_6 \right)}{\left((1 + \epsilon w_4) + \frac{Rd}{A_3} \right)}, \quad (23)$$

$$\phi' = w_7, \quad (24)$$

$$\phi'' = \beta_1 Sc(1 + \delta w_4)^n \exp\left(\frac{-E}{1 + \delta w_4}\right) w_6 - \left(\frac{Nt}{Nb}\right) w_6' - Sc w_1 w_7, \quad (25)$$

$$\left. \begin{array}{l} \eta = 0 : w_1(\eta) = 0, w_2(\eta) = \lambda, w_4 = 1, w_6 = 1, \\ \eta \rightarrow \infty : w_2(\eta) \rightarrow 1, w_4(\eta) \rightarrow 0, w_6(\eta) \rightarrow 0. \end{array} \right\} \quad (26)$$

5. Step-By-Step Graphical Detail of the Present Problem

The step-by-step graphical representation of the LobattoIIIA MATLAB builtin numerical scheme is given below.

5.1. Problem Formulation

The nonlinear PDEs with the inclusion of different effects are mentioned below (Figure 3a).

5.2. Modelling

The nonlinear PDEs are transmuted into dimensionless ODEs by the utilization of similarity variables (Figure 3b) derived from the boundary layer theory approximations and stream functions related to the fluid flow over a flat plate.

5.3. Numerical Process

The mathematical expressions of the dimensionless ODEs regarding momentum, temperature, and concentration equations are enumerated below (Figure 3c).

5.4. Numerical Results

The numerical effect of different dimensionless components discovered during the computational analysis of the issue versus rapidity, heat, and concentration was computed and is displayed in the form of charts and tables. The skin friction coefficient, as well as heat transfer Nusselt number, were also computed numerically. The graphical representation is given below (Figure 3d).

5.5. Analysis

In the end, the accuracy of obtained results was also checked numerically with the already available literature.

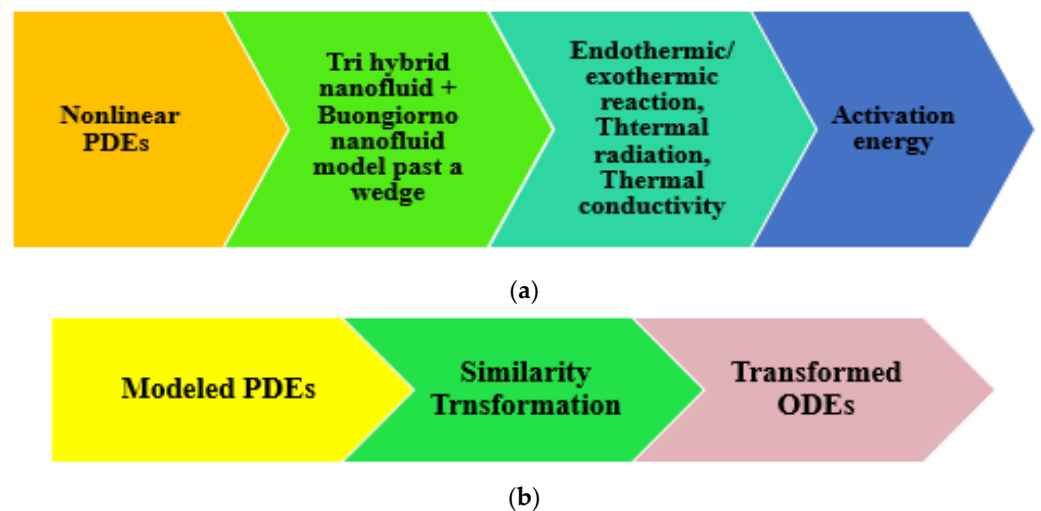


Figure 3. Cont.

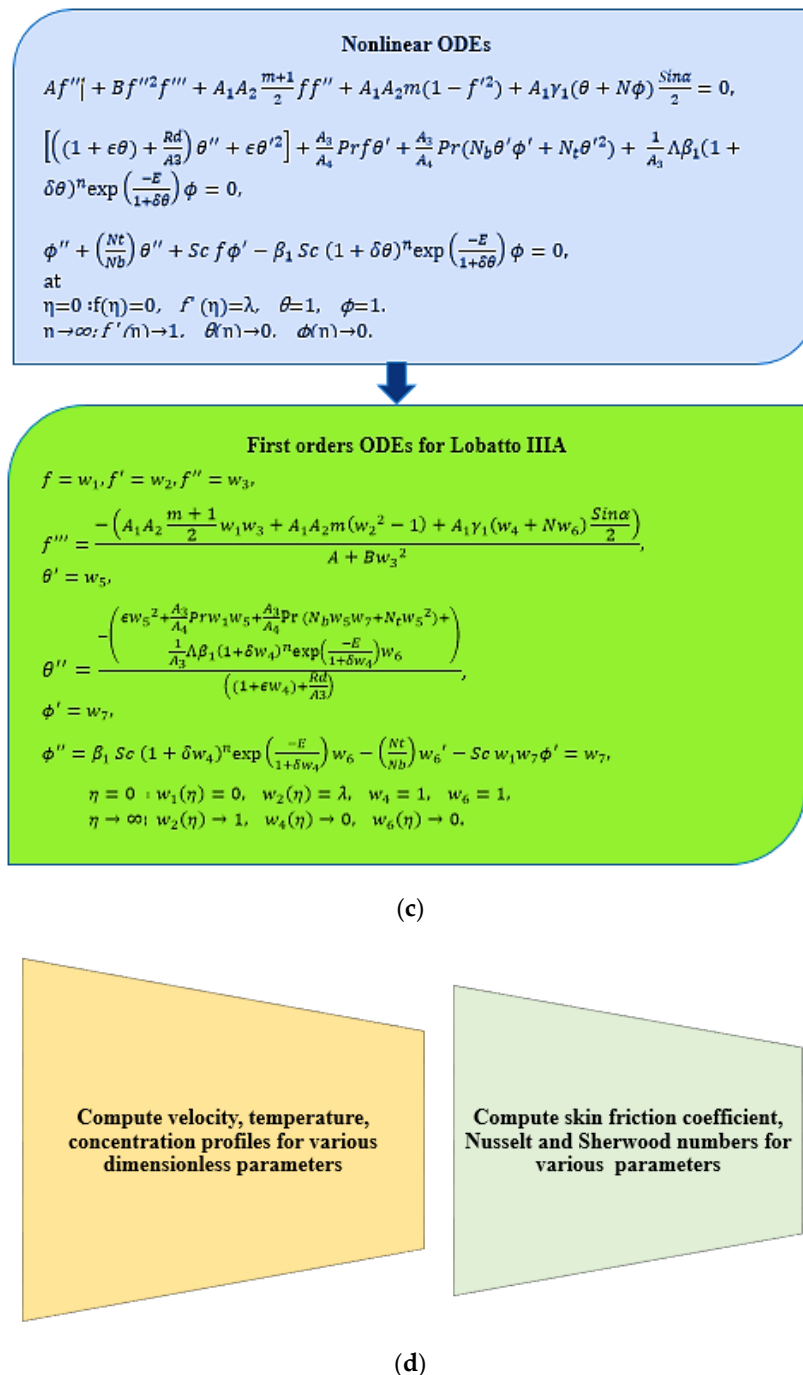


Figure 3. (a). Novel effects. (b). Transformation step. (c). Numerical process. (d). Computed quantities.

6. Results and Discussions

The modeled nonlinear PDEs are converted into ODEs and these equations numerically with the support of Lobatto III A MATLAB constructed in the bvp4c scheme. These numerical outcomes are portrayed and discussed theoretically and numerically in the form of figures and tables in this section.

Figure 4 is designed to study the impression of fluid variable A on the rapidity outlines. It is quite evident that amplification in the fluid parameter denigrates the liquid viscidness and magnifies the liquid rapidity. As a result, the velocity profile escalates.

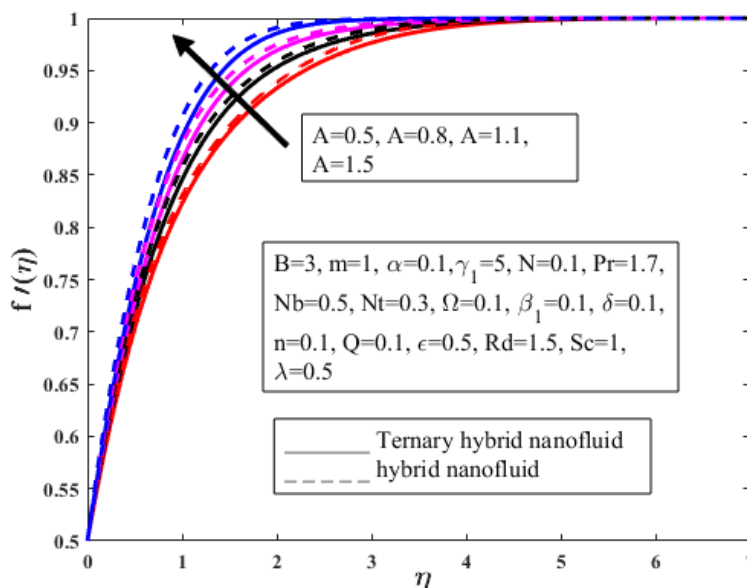


Figure 4. Activity change of A on $f'(\eta)$.

Figure 5 reveals the inspiration of elastic variable B on the rapidity outlines. It is noted that the addition of tri-hybrid nanomolecules in the standard liquid (EG) augments the thermic performance of the liquid which eventually lessens the fluid viscosity and augments the liquid rapidity. The effect of wedge factor m on the rapidity field is highlighted in Figure 6. The surface area of the wedge increases owing to magnification in m . As a result, more fluid is moving over the wedge surface which amplifies the fluid velocity. A positive variation in m improves a satisfactory pressure difference which amplifies the fluid velocity. Figure 7 illustrates that a significant change in wedge angle parameter α brings about a decrement in liquid rapidity. The impression of the buoyancy ratio factor γ_1 on the rapidity, the field is demonstrated in Figure 8. Buoyancy forces dominate the viscous forces by the virtue of magnification in γ_1 . Grashof number is directly related to the viscous forces. It is observed that a constructive disparity in γ_1 augments the liquid density, which depreciates the Grashof number and the fluid velocity.

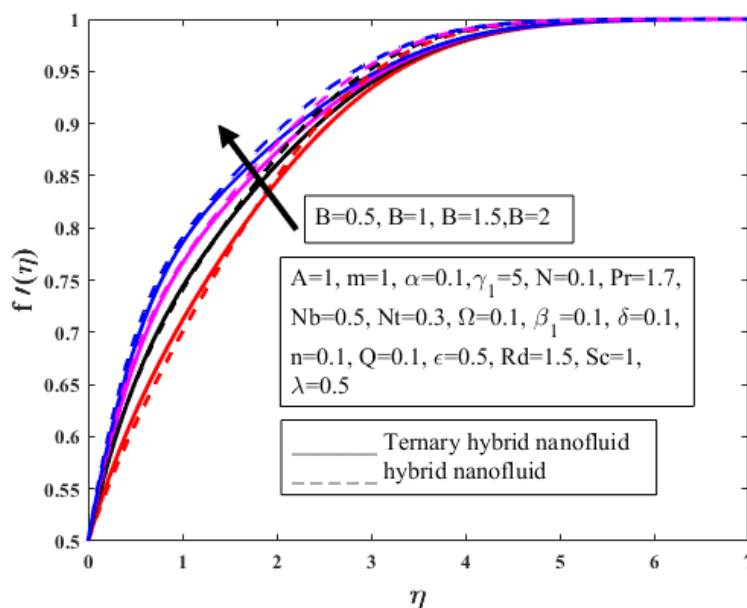


Figure 5. Activity change of B on $f'(\eta)$.

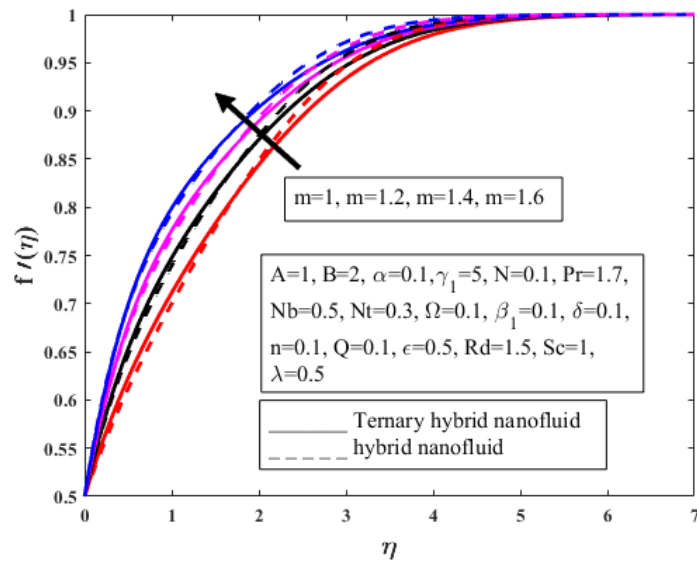


Figure 6. Activity change of m on $f'(\eta)$.

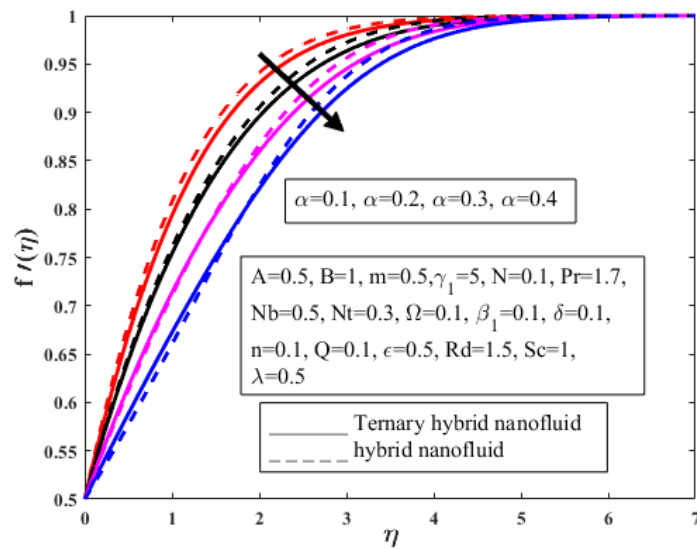


Figure 7. Activity change of α on $f'(\eta)$.

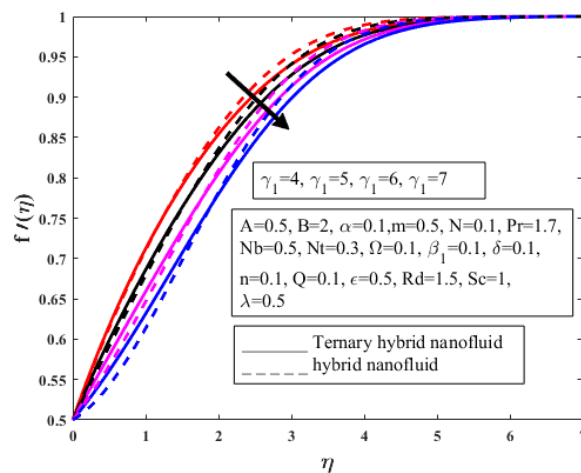


Figure 8. Activity change of γ_1 on $f'(\eta)$.

Figure 9 is designed to reflect the impression of λ on the velocity field. The parameter λ is actually dependent on the buoyancy forces. It is remarked that the buoyancy powers dominate the viscid powers owing to an increment in λ which amplifies the fluid movement over the surface and amplifies the velocity field. The Brownian's diffusion Nb effect on the temperature field is highlighted in Figure 10. The insertion of nanomolecules in the standard liquid boosts the fluid temperature. Heat transmission rate of the fluid increases. Molecules of the fluid strike beyond at random by the integrity of enlargement in Nb and the mean kinetic energy of particle boosts, which amplifies the fluid temperature and the temperature outline. Figure 11 depicts the escalating effect of Nt on $\theta(\eta)$. Incremental change in nanoparticle diffusion amplifies $\theta(\eta)$. The thermophoresis diffusion phenomenon migrates the hot fluid molecules from the warm region to the icy zone. As a result, the temperature field increases. Figures 12 and 13 visualize the performance of the endothermic/exothermic reaction parameter on $\theta(\eta)$. In the case of $\Omega > 0$, heat is released by a system, which creates a reduction in the liquid temperature as shown in Figure 11, but the reverse comportment is remarked in the status of Figure 13. The heat is absorbed by the fluid in the case of $\Omega < 0$. Heat transfer rate amplifies, which furthermore enhances $\theta(\eta)$. From Figure 14, it is noticed that the temperature field augments owing to an incremental change in the reaction rate parameter β_1 . It is observed that a positive change in β_1 brings about an amplification in $\beta_1(1 + \delta\theta)^n \exp\left(\frac{-E}{1+\delta\theta}\right)$. As a result, a constructive chemical reaction takes place which enhances the heat transfer rate and $\theta(\eta)$.

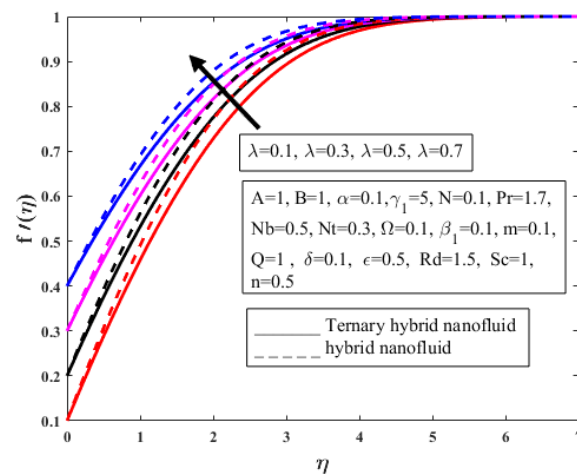


Figure 9. Activity change of λ on $f'(\eta)$.

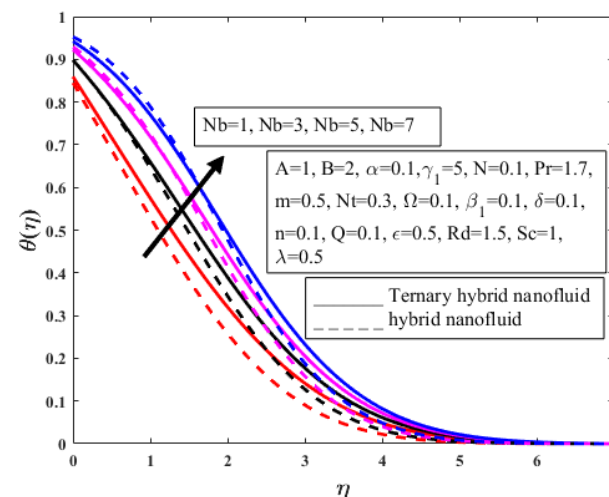


Figure 10. Activity change of Nb on $\theta(\eta)$.

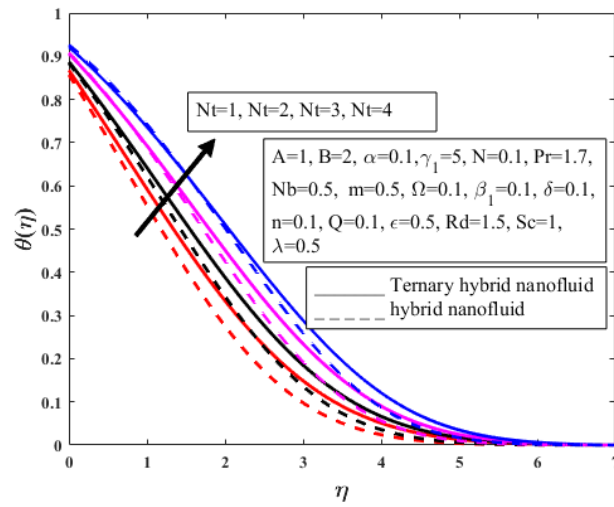


Figure 11. Activity change of Nt on $\theta(\eta)$.

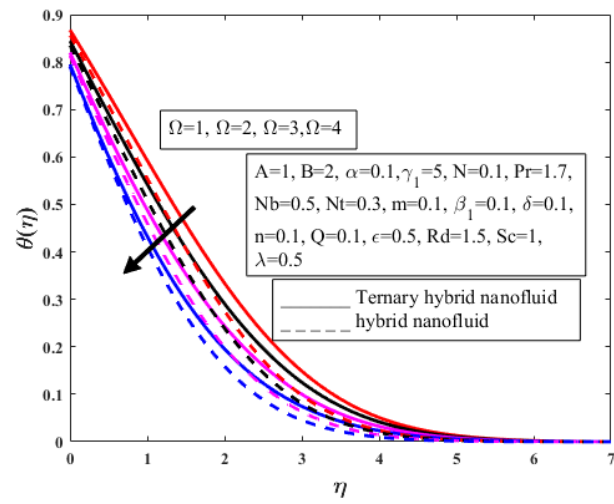


Figure 12. Activity change of Ω on $\theta(\eta)$.

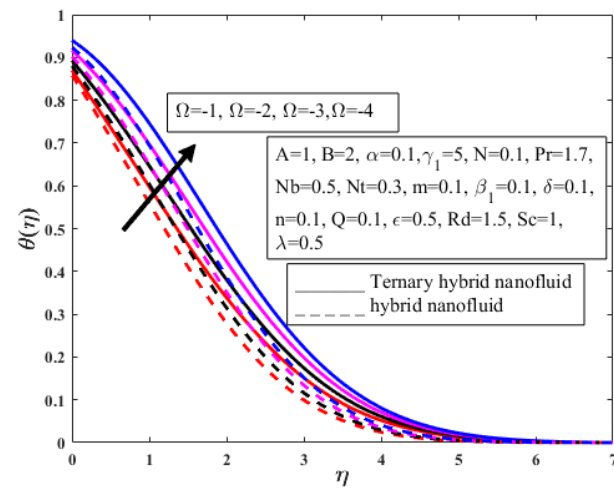


Figure 13. Activity change of Ω on $\theta(\eta)$.

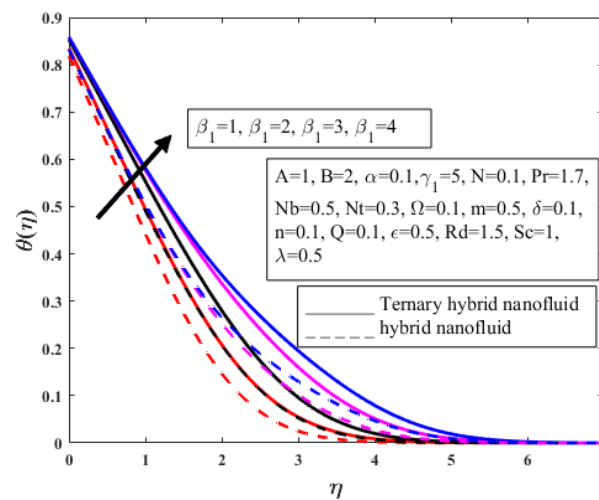


Figure 14. Activity change of β_1 on $\theta(\eta)$.

From Figure 15, it can be shown that the radiating factor Rd has a temperature-enhancing impact. Thermal radiation is employed where a substantial temperature differential is necessary, such as in combustible reactors, nuclear reactors, polymeric synthesis, and so on. Inserting nanomaterials into the conventional fluids and augmenting Rd improves the fluid's rate of heat transmission and temperature field $\theta(\eta)$. It is observed from Figure 16 that an amplification in thermal conductivity ϵ amplifies the temperature. The competence of any matter to conduct heat is described as thermal conducting. In fluids, thermal conducting is amplified because of a collision of the molecules. The insertion of nanomolecules in the standard liquid boosts the fluid collision capacity to generate more heat which eventually escalates the heat transfer rate and $\theta(\eta)$. The influence of the active energy factor on $\theta(\eta)$ is displayed in Figure 17. The minimum energy necessary to start a chemically reactive process is known as active energy. It is crystal clear that a constructive variant in Q strengthens the liquid concentration and depreciates the thermal performance of the fluid. As a result, heat transmission in addition to the temperature inside the fluid depreciates. The consequences of power-law index n on $\theta(\eta)$ are delineated in Figure 18. It is noteworthy that an augmentation in power-law index n amplifies the fluid concentration and brings about an enhancement in fluid temperature. Figure 19 delineated the effect of temperature difference parameter δ on $\theta(\eta)$. The gap between the temperature of the sheet and the free streaming temperature increases which slows down the liquid temperature and heat transmission rate. The influence of Sc on the concentricity outline is displayed in Figure 20. Sc is the ratio of motion diffusion to mass diffusion. From the figure, it is observed that magnification in mass diffusivity brings about a decrement in the concentration of nanoparticles which ultimately guides to a decrement in the concentricity outline. The impact of Nb on the concentricity outline is displayed in Figure 21. It is the noteworthy concentration of nanoparticles that increases as a result of amplification in Nb . As a result, the concentration of nanoparticles and the mass fraction field diminishes. From Figure 22 it is observed that the mass fraction field escalates owing to magnification in Nt . The molecules migrate the region of the hotter surface towards the colder one which depreciates the fluid temperature and magnifies the concentration field. Figure 23 is designed to study the influence of activation energy Q on the concentricity fractional outline $\phi(\eta)$. It is quite evident that magnification in Q depreciates $(1 + \delta\theta)^n \exp\left(\frac{-E}{1+\delta\theta}\right)\phi$. As a result, the concentration field decreases. It is observed from Figure 24 that magnification in the temperature difference parameter depreciates the fluid concentration and mass fraction field.

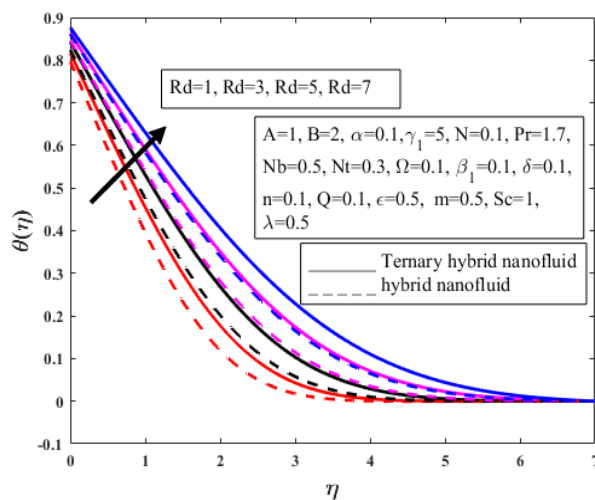


Figure 15. Activity change of Rd on $\theta(\eta)$.

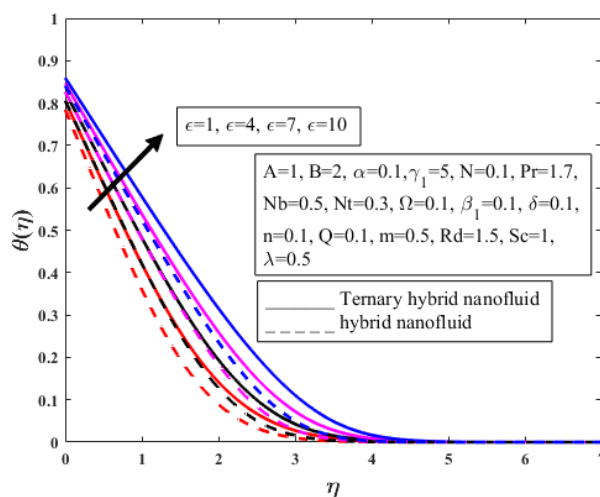


Figure 16. Activity change of ϵ on $\theta(\eta)$.

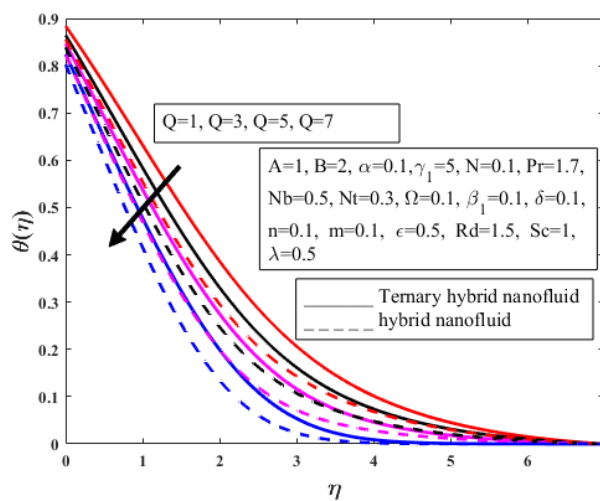


Figure 17. Activity change of Q on $\theta(\eta)$.

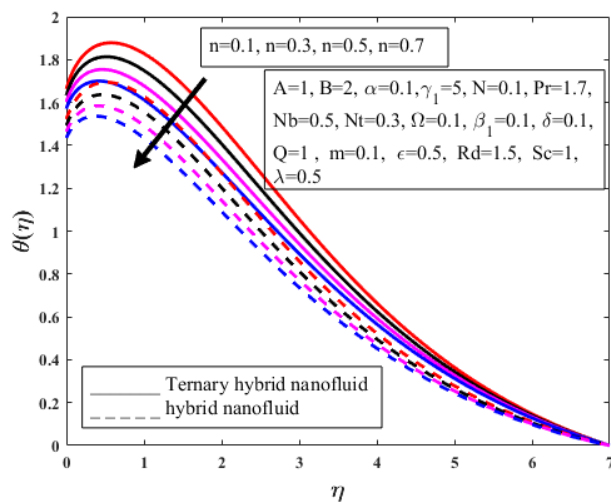


Figure 18. Activity change of n on $\theta(\eta)$.

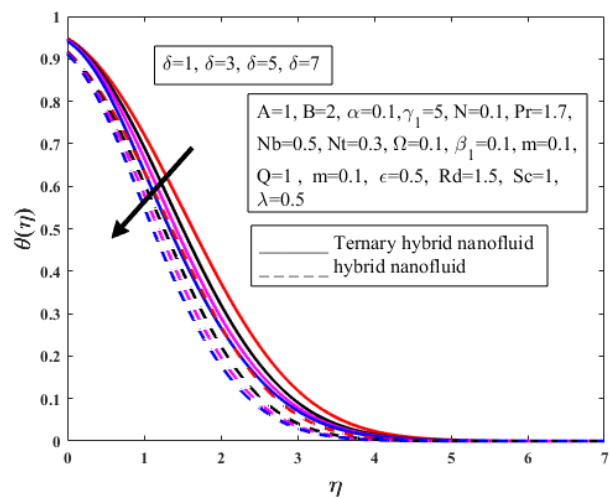


Figure 19. Activity change of δ on $\theta(\eta)$.

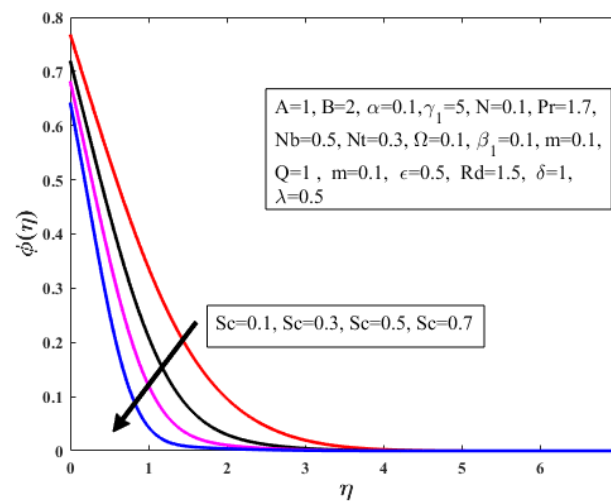


Figure 20. Activity change of Sc on $\phi(\eta)$.

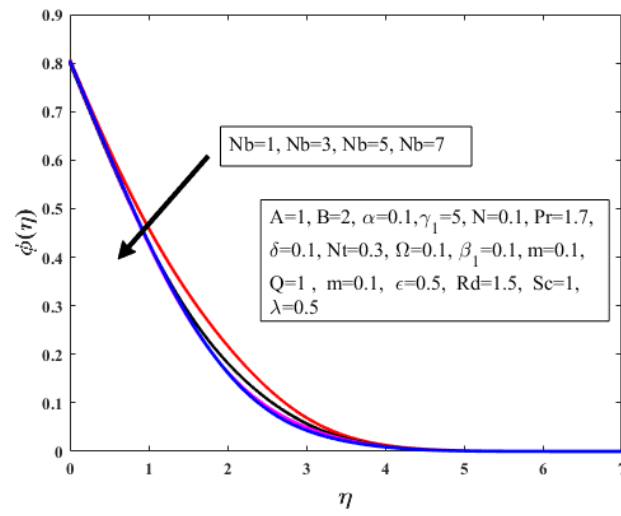


Figure 21. Activity change of Nb on $\phi(\eta)$.

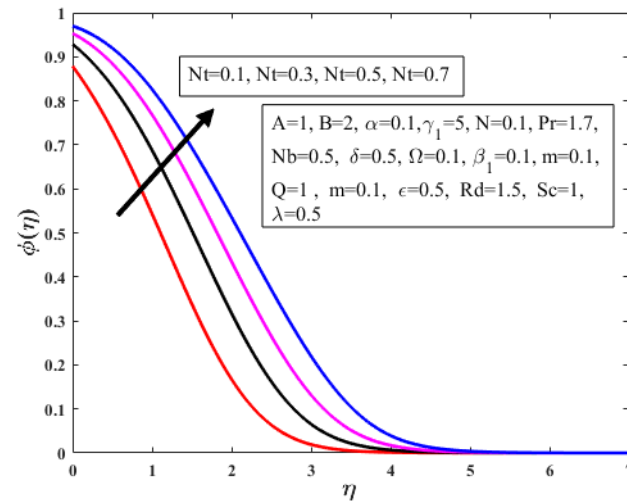


Figure 22. Activity change of Nt on $\phi(\eta)$.

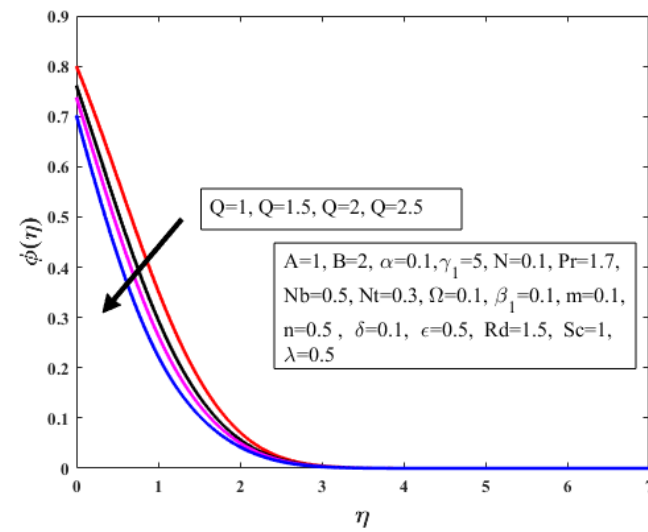


Figure 23. Activity change of Q on $\phi(\eta)$.

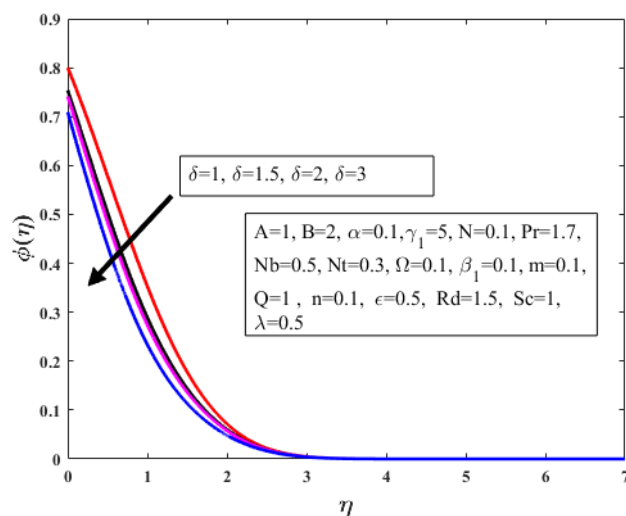


Figure 24. Activity change of Q on $\phi(\eta)$.

Table 2 is designed to study the comparative analysis of obtained results with Refs. [38–40] for the status of a constructive variant in wedge factor. From Table 2, it is crystal clear that the obtained results are quite promising. Table 3 is planned to analyze the performance of diverse factors on the wall frictional factor. From Table 3 it is observed that an augmentation in buoyancy ratio γ_1 , wedge angle at the surface λ , consternation parameter N , reaction rate β_1 bring about amplification in the frictional factor. From Table 4, it is observed that an incremental change in thermal conductivity ϵ , thermal radiation Rd , Prandtl number Pr , and Brownian motion Nb , provide a substantial increment in heat transfer Nusselt number. The heat transmission rate diminishes by the advantage of amplification in endothermic/exothermic reaction parameter Ω , the reaction rate β_1 and Schmidt number, temperature difference δ , power-law index n , and activation energy. It is noted that an augmentation in ϵ , Rd , Nt , Ω , n escalate the heat transmission rate, but the opposite behavior is reported in the situation of residual factors such as Pr , β_1 , Sc , Nb , Q , δ .

Table 2. Comparison analysis of the obtained results with existing literature for the case of $f''(0)$ for various values of m .

m	Ref. [38]	Ref. [39]	Ref. [40]	Present Results
0.0	0.46960	0.46960	0.46961	0.46970
0.1	0.65510	0.65511	0.65509	0.65510
0.2	0.80210	0.80210	0.80211	0.80221
0.3	0.92760	0.92760	0.92771	0.92780
0.5	1.03850	1.03860	1.03892	1.03911
1.0	1.13250	1.23260	1.23261	1.23282

Table 3. Values of sundry parameters on the skin friction coefficient.

Parameters	Skin Friction
$\gamma_1 = 0.2$	6.03433
$\gamma_1 = 0.4$	6.03418
$\gamma_1 = 0.4$	6.03406
$\lambda = -0.2$	6.17675
$\lambda = 0.0$	7.33591
$\lambda = 0.2$	8.26719
$N = 0.2$	7.89913
$N = 0.4$	9.66534
$N = 0.6$	11.45915
$\beta_1 = 1.0$	7.28419

Table 3. Cont.

Parameters	Skin Friction
$\beta_1 = 2.0$	7.35732
$\beta_1 = 3.0$	7.68177

Table 4. Effect of dimensionless parameters on heat and mass transfer rates.

ϵ	Rd	Pr	Nb	Nt	Ω	β_1	δ	n	Q	Sc	$Nu_x Re_x^{1/2}$	$Sh_x Re_x^{1/2}$
1	1	1.7	1	0.5	0.1	0.1	0.1	0.1	0.1	0.5	4.9383	2.3428
2											5.9218	2.3437
3											6.9050	2.3448
4											7.8888	2.3458
	2										4.1025	3.3490
	3										5.7546	3.3534
	4										6.3993	3.3967
		3									3.0691	2.3342
		4									3.5236	1.9310
		5									4.1573	1.3294
			2								4.8302	3.3665
			3								5.7312	2.3740
			4								6.6413	1.3774
				1							3.8959	2.3150
				1.5							2.8556	1.9948
				2							1.8173	1.2814
					0.3						2.9229	2.3443
					0.5						1.9074	2.3459
					0.7						0.8920	2.3475
						0.3					3.9246	2.3110
						0.5					2.9114	2.2779
						0.7					1.8987	2.2496
							0.3				3.9387	2.3437
							0.5				2.9391	3.3545
							0.7				1.9395	4.4454
								0.3			4.9384	3.3460
								0.5			3.9400	2.3528
								0.7			2.9596	1.3776
									0.3		6.9396	3.3457
									0.5		5.9406	4.3480
									0.7		4.9415	5.3500
										1	2.9262	4.4540
										1.5	2.8827	3.5228
										2	2.7218	2.5726

7. Testing of Code

Table 2 is designed to present the comparative analysis of the obtained results with Yacob et al. [38], White [39], and Ali et al. [40] in the case of surface drag coefficient $f''(0)$ owing to magnification in wedge parameter m . The comparison with the already available literature on the wedge has been made by keeping elastic parameter $B = 0$, wedge angle $\alpha = 0$, buoyancy parameter $\gamma_1 = 0$, $\phi_1 = \phi_2 = \phi_3 = 0$, nanofluid viscosity $A_1 = 1$, nanofluid density $A_2 = 1$, and stagnation parameter $\lambda = 1$. From the comparison, it is crystal clear that the obtained results are quite promising and authentic. It is also clear that the proposed numerical analysis is quite robust and reliable.

From Figure 25, it is noticed that a positive variation in the buoyancy parameter amplifies the mass transfer rate, but no change is remarked in the case of frictional force and the transmission rate. Figure 26 demonstrates the incremental change in porosity medium and parameter λ brings about a magnification in the wall frictional force but transmission rates remain unchanged. The frictional force factor, mass transfer and extra heat transmission

rate are augmented by virtue of an incremental change in the sustentation parameter N as shown in Figure 27. From Figure 28, it is detected that magnification in the reactive rate constant parameter provides a substantial change in the surface drag coefficient.

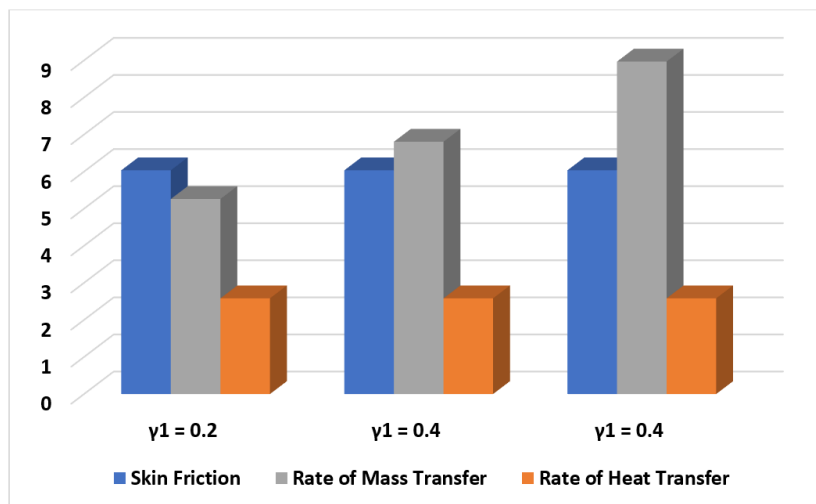


Figure 25. Influence of γ_1 on skin friction, heat transfer, and mass transfer rates.

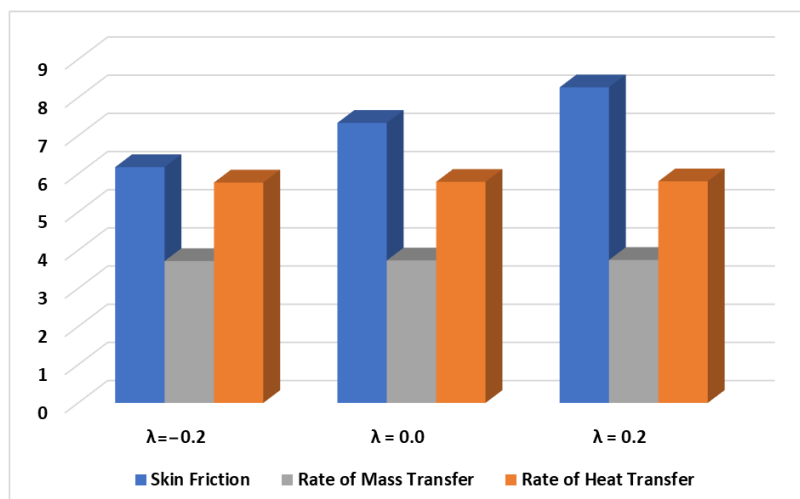


Figure 26. Influence of λ on skin friction, heat transfer, and mass transfer rate.

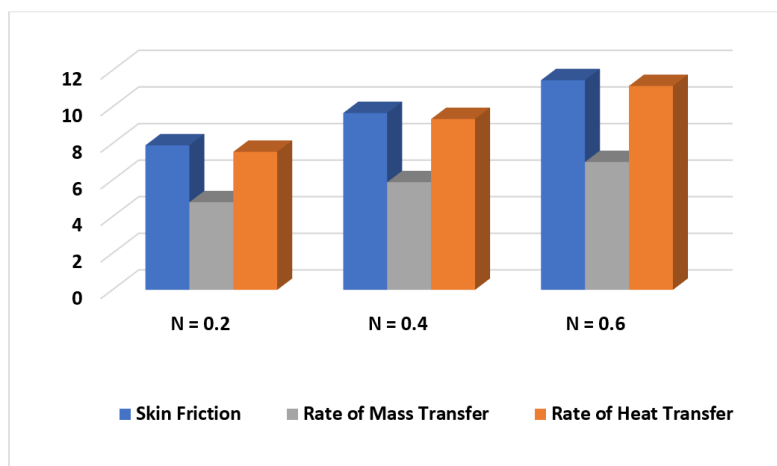


Figure 27. Influence of N on skin friction, heat transfer, and mass transfer rate.

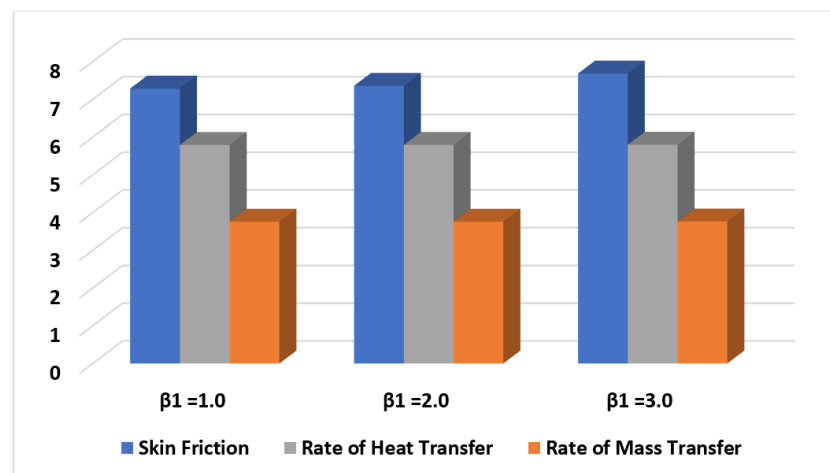


Figure 28. Influence of β_1 on skin friction, heat transfer, and mass transfer rate.

8. Concluding Remarks

The following summarizes the conclusions of our study:

- The addition of tri-hybrid nanomolecules in the standard liquid boosts the thermal performance of the liquid which eventually lessens the fluid viscosity;
- The amplification in the fluid parameter B devalues the liquid viscidness and upsurges the liquid rapidity.
- A larger wedge m brings about magnification in fluid viscosity contributing to viscous forces dominating the shear forces and depreciating the velocity field.
- Wedge angle parameter α brings about a decrement in fluid velocity. Amplification in α provides resistance to the fluid which helps the fluid to become denser and more viscous. As a result, the velocity field diminishes.
- Buoyancy forces dominate the viscous forces by virtue of magnification in the buoyancy parameter γ_1 . Positive variation in buoyancy parameter γ_1 amplifies the fluid density which depreciates the Grashoff number Gr and the fluid velocity.
- Thermophoresis diffusion phenomenon N_t migrates the hot fluid molecules from the warm region to the coldish zone. As a result, the temperature field increases.
- In the case of exothermic reaction $\Omega > 0$, heat is released by a system that gives a reduction in the liquid temperature. Examples are fuel combustion, heat pumps, heat engines, refrigerators, etc. Heat is absorbed by the fluid in the case of exothermic reaction $\Omega < 0$. Examples are absorption chillers, ammonia absorption refrigeration systems, photosynthesis, etc.
- Chemical reaction takes place which enhances the heat transfer rate and $\theta(\eta)$. Physical examples are the combustion of fuels, detonation of explosives, reaction of acids with metals, etc.
- Amplification in thermal conductivity ϵ amplifies the temperature. That is why the insertion of copper nanoparticles instead of any other sort of nanoparticles delivers more heat because they have more thermal conductivity than other metallic nanoparticles.
- Positive variation in activation energy Q amplifies the fluid concentration and depreciates the thermal performance of the fluid. Enzyme reactions are a good example of activation energy.
- It is noted that an augmentation in thermal conductivity ϵ , thermal radiation Rd , thermophoresis parameter Nt , endothermic/exothermic reaction Ω , and fitted rate n escalate the heat transmission rate, while the opposite behavior is reported in the status of keeping factors such as Prandtl number Pr , β_1 , Schmidt number Sc , Brownian parameter Nb , activation energy Q , temperature difference δ .

The Lobatto III A structure scheme could be applied to a variety of physical and technical challenges in the future [41–43]. Some recent developments exploring the significance of the considered research domain have been reported by [44–50].

Author Contributions: Conceptualization, T.S., A.A., S.Z.H.S., W.J. and M.R.E.; methodology, T.S., A.A., W.J. and M.R.E.; software, M.R.E., E.S.M.T.E.D., R.I. and S.M.H.; validation, W.J., M.R.E. and S.M.H.; formal analysis, T.S., A.A., S.Z.H.S. and M.R.E.; investigation, W.J. and M.R.E.; resources, T.S., S.Z.H.S. and E.S.M.T.E.D.; data curation, M.R.E., R.I. and S.M.H.; writing—original draft preparation, W.J. and M.R.E.; writing—review and editing, A.A., W.J. and M.R.E.; visualization, W.J. and S.M.H.; supervision, W.J.; project administration, M.R.E.; funding acquisition, S.M.H. All authors have read and agreed to the published version of the manuscript.

Funding: This research was funded by Deanship of Scientific Research, Islamic University of MaDinah, Ministry of Education, KSA grant number Research Group Program/1/804.

Institutional Review Board Statement: Not applicable.

Informed Consent Statement: Not applicable.

Acknowledgments: Authors are grateful to the Deanship of Scientific Research, Islamic University of MaDinah, Ministry of Education, KSA for supporting this research work through research project grant under Research Group Program/1/804.

Conflicts of Interest: The authors declare no conflict of interest.

Nomenclature

Q	activation energy	δ	temperature difference
n	power law indicator	Nt	thermophoretic diffusion
Nb	Brownian diffusion	B	elastic parameter
γ_1	buoyancy parameter	Gr	Grashof quantity
ϵ	thermal conductivity	Cf_x	Frictional force
β_1	reaction rate	Rd	radiative variable
Pr	Prandtl number	q_r	radiant heat fluxing
N	Sustentation factor	A	Prandtl fluid parameter
λ	buoyancy ratio parameter	α_{thnf}	thermal diffusion
ρ_{thnf}	consistency	k_{thnf}	thermal conducting
C_p	specific heat	κ^*	absorbed factor
σ^*	Stefan-Boltzmann value		

References

- Ahmad, S.; Nadeem, S. Analysis of activation energy and its impact on hybrid nanofluid in the presence of Hall and ion slip currents. *Appl. Nanosci.* **2020**, *10*, 5315–5330. [[CrossRef](#)]
- Waqas, H.; Khan, S.U.; Tlili, I.; Awais, M.; Shadloo, M.S. Significance of bioconvective and thermally dissipation flow of viscoelastic nanoparticles with activation energy features: Novel biofuels significance. *Symmetry* **2020**, *12*, 214. [[CrossRef](#)]
- Owhaib, W.; Basavarajappa, M.; Al-Kouz, W. Radiation effects on 3D rotating flow of Cu-water nanoliquid with viscous heating and prescribed heat flux using modified Buongiorno model. *Sci. Rep.* **2021**, *11*, 20669. [[CrossRef](#)] [[PubMed](#)]
- Rosca, N.C.; Rosca, A.V.; Aly, E.H.; Pop, I. Flow and Heat Transfer Past a Stretching/Shrinking Sheet Using Modified Buongiorno Nanoliquid Model. *Mathematics* **2021**, *9*, 3047. [[CrossRef](#)]
- Rana, P.; Gupta, G. Numerical and sensitivity computations of three-dimensional flow and heat transfer of nanoliquid over a wedge using modified Buongiorno model. *Comput. Math. Appl.* **2021**, *101*, 51–62. [[CrossRef](#)]
- Mousavi, S.; Esmailzadeh, F.; Wang, X. Effects of temperature and particles volume concentration on the thermophysical properties and the rheological behavior of CuO/MgO/TiO₂ aqueous ternary hybrid nanofluid. *J. Therm. Anal. Calorim.* **2019**, *137*, 879–901. [[CrossRef](#)]
- Dezfulizadeh, A.; Aghaei, A.; Joshaghani, A.H.; Najafzadeh, M.M. An experimental study on dynamic viscosity and thermal conductivity of water-Cu-SiO₂-MWCNT ternary hybrid nanofluid and the development of practical correlations. *Powder Technol.* **2021**, *389*, 215–234. [[CrossRef](#)]
- Munjam, S.R.; Gangadhar, K.; Seshadri, R.; Rajeswar, M. Novel technique MDDIM solutions of MHD flow and radiative Prandtl-Eyring fluid over a stretching sheet with convective heating. *Int. J. Ambient. Energy* **2021**, 1–10. [[CrossRef](#)]
- Ullah, I.; Ali, R.; Nawab, H.; Abdussatar; UdDin, I.; Muhammad, T.; Khan, I.; Nisar, K.S. Theoretical analysis of activation energy effect on Prandtl-Eyring nanoliquid flow subject to melting condition. *J. Non-Equil. Thermodyn.* **2022**, *47*, 1–12. [[CrossRef](#)]

10. Qureshi, M.A. A case study of MHD driven Prandtl-Eyring hybrid nanofluid flow over a stretching sheet with thermal jump conditions. *Case Stud. Therm. Eng.* **2021**, *28*, 101581. [[CrossRef](#)]
11. Shah, S.Z.; Wahab, H.A.; Ayub, A.; Sabir, Z.; Haider, A.; Shah, S.L. Higher order chemical process with heat transport of magnetized cross nanofluid over wedge geometry. *Heat Transf.* **2021**, *50*, 3196–3219. [[CrossRef](#)]
12. Ayub, A.; Darvesh, A.; Altamirano, G.C.; Sabir, Z. Nanoscale energy transport of inclined magnetized 3D hybrid nanofluid with Lobatto IIIA scheme. *Heat Transf.* **2021**, *50*, 6465–6490. [[CrossRef](#)]
13. Al-Hossainy, A.F.; Eid, M.R. Combined experimental thin films, TDDFT-DFT theoretical method, and spin effect on [PEG-H₂O/ZrO₂+MgO] hybrid nanofluid flow with higher chemical rate. *Surf. Interfaces* **2021**, *23*, 100971. [[CrossRef](#)]
14. Ayub, A.; Sabir, Z.; Shah, S.Z.H.; Wahab, H.A.; Sadat, R.; Ali, M.R. Effects of homogeneous-heterogeneous and Lorentz forces on 3-D radiative magnetized cross nanofluid using two rotating disks. *Int. Commun. Heat Mass Transf.* **2022**, *130*, 105778. [[CrossRef](#)]
15. Ali, L.; Ali, B.; Liu, X.; Iqbal, T.; Zulqarnain, R.M.; Javid, M. A comparative study of unsteady MHD Falkner–Skan wedge flow for non-Newtonian nanofluids considering thermal radiation and activation energy. *Chin. J. Phys.* **2022**, *77*, 1625–1638. [[CrossRef](#)]
16. Ayub, A.; Sabir, Z.; Shah, S.Z.H.; Mahmoud, S.; Algarni, A.; Sadat, R.; Ali, M.R. Aspects of infinite shear rate viscosity and heat transport of magnetized Carreau nanofluid. *Eur. Phys. J. Plus* **2022**, *137*, 247. [[CrossRef](#)]
17. Neethu, T.; Sabu, A.; Mathew, A.; Wakif, A.; Areekara, S. Multiple linear regression on bioconvective MHD hybrid nanofluid flow past an exponential stretching sheet with radiation and dissipation effects. *Int. Commun. Heat Mass Transf.* **2022**, *135*, 106115. [[CrossRef](#)]
18. Shah, S.Z.H.; Fathurrochman, I.; Ayub, A.; Altamirano, G.C.; Rizwan, A.; Núñez, R.A.S.; Sabir, Z.; Yeskindirova, M. Inclined magnetized and energy transportation aspect of infinite shear rate viscosity model of Carreau nanofluid with multiple features over wedge geometry. *Heat Transf.* **2022**, *51*, 1622–1648. [[CrossRef](#)]
19. Shah, S.L.; Ayub, A.; Dehraj, S.; Wahab, H.A.; Sagayam, K.M.; Ali, M.R.; Sadat, R.; Sabir, Z. Magnetic dipole aspect of binary chemical reactive Cross nanofluid and heat transport over composite cylindrical panels. *Waves Random Complex Media* **2022**, 1–24. [[CrossRef](#)]
20. Sandeep, N.; Ranjana, B.; Samrat, S.; Ashwinkumar, G. Impact of nonlinear radiation on magnetohydrodynamic flow of hybrid nanofluid with heat source effect, P.I. *Proc. Inst. Mech. Eng. Part E J. Process Mech. Eng.* **2022**, *236*, 1616–1627. [[CrossRef](#)]
21. Ellahi, R.; Zeeshan, A.; Hussain, F.; Asadollahi, A. Peristaltic blood flow of couple stress fluid suspended with nanoparticles under the influence of chemical reaction and activation energy. *Symmetry* **2019**, *11*, 276. [[CrossRef](#)]
22. Khan, A.A.; Bukhari, S.R.; Marin, M.; Ellahi, R. Effects of chemical reaction on third-grade MHD fluid flow under the influence of heat and mass transfer with variable reactive index. *Heat Transf. Res.* **2019**, *50*, 1061–1080. [[CrossRef](#)]
23. Vijaya, N.; Arifuzzaman, S.; Sai, N.R.; Rao, M. Analysis of Arrhenius activation energy in electrically conducting Casson fluid flow induced due to permeable elongated sheet with chemical reaction and viscous dissipation. *Front. Heat Mass Transf.* **2020**, *15*, 26. [[CrossRef](#)]
24. Ali, Z.; Zeeshan, A.; Bhatti, M.; Hobiny, A.; Saeed, T. Insight into the dynamics of Oldroyd-B fluid over an upper horizontal surface of a paraboloid of revolution subject to chemical reaction dependent on the first-order activation energy. *Arab. J. Sci. Eng.* **2021**, *46*, 6039–6048. [[CrossRef](#)]
25. Zaib, A.; Haq, R.U.; Sheikholeslami, M.; Khan, U. Numerical analysis of effective Prandtl model on mixed convection flow of γ Al₂O₃-H₂O nanoliquids with micropolar liquid driven through wedge. *Phys. Scr.* **2020**, *95*, 035005. [[CrossRef](#)]
26. Habib, D.; Salamat, N.; Abdal, S.H.S.; Ali, B. Numerical investigation for MHD Prandtl nanofluid transportation due to a moving wedge: Keller box approach. *Int. Commun. Heat Mass Transf.* **2022**, *35*, 106141. [[CrossRef](#)]
27. Shah, Z.; Kumam, P.; Deebani, W. Radiative MHD Casson Nanofluid Flow with Activation energy and chemical reaction over past nonlinearly stretching surface through Entropy generation. *Sci. Rep.* **2020**, *10*, 4402. [[CrossRef](#)]
28. Bhatti, M.; Michaelides, E.E. Study of Arrhenius activation energy on the thermo-bioconvection nanofluid flow over a Riga plate. *J. Therm. Anal. Calorim.* **2021**, *143*, 2029–2038. [[CrossRef](#)]
29. Gowda, R.J.P.; Kumar, R.N.; Jyothi, A.M.; Prasannakumara, B.C.; Sarris, I.E. Impact of binary chemical reaction and activation energy on heat and mass transfer of marangoni driven boundary layer flow of a non-Newtonian nanofluid. *Processes* **2021**, *9*, 702. [[CrossRef](#)]
30. Ullah, Z.; Ullah, I.; Zaman, G.; Sun, T.C. A numerical approach to interpret melting and activation energy phenomenon on the magnetized transient flow of Prandtl–Eyring fluid with the application of Cattaneo–Christov theory. *Waves Random Complex Media* **2022**, 1–21. [[CrossRef](#)]
31. Habib, D.; Salamat, N.; Abdal, S.; Siddique, I.; Ang, M.C.; Ahmadian, A. On the role of bioconvection and activation energy for time dependent nanofluid slip transpiration due to extenDing domain in the presence of electric and magnetic fields. *Ain Shams Eng. J.* **2022**, *13*, 101519. [[CrossRef](#)]
32. Asogwa, K.K.; Alsulami, M.; Prasannakumara, B.; Muhammad, T. Double diffusive convection and cross diffusion effects on Casson fluid over a Lorentz force driven Riga plate in a porous medium with heat sink: An analytical approach. *Int. Commun. Heat Mass Transf.* **2022**, *131*, 105761. [[CrossRef](#)]
33. Ali, U.; Rehman, K.U.; Malik, M.; Zehra, I. Thermal aspects of Carreau fluid around a wedge. *Case Stud. Therm. Eng.* **2018**, *12*, 462–469. [[CrossRef](#)]
34. Lyu, H.-G.; Deng, R.; Sun, P.-N.; Miao, J.-M. Study on the wedge penetrating fluid interfaces characterized by different density-ratios: Numerical investigations with a multi-phase SPH model. *Ocean Eng.* **2021**, *237*, 109538. [[CrossRef](#)]

35. Hussain, M.; Ghaffar, A.; Ali, A.; Shahzad, A.; Nisar, K.S.; Alharthi, M.; Jamshed, W. MHD thermal boundary layer flow of a Casson fluid over a penetrable stretching wedge in the existence of nonlinear radiation and convective boundary condition. *Alex. Eng. J.* **2021**, *60*, 5473–5483. [[CrossRef](#)]
36. Waqas, H.; Farooq, U.; Bhatti, M.M.; Hussain, S. Magnetized bioconvection flow of Sutterby fluid characterized by the suspension of nanoparticles across a wedge with activation energy. *ZAMM J. Appl. Math. Mech.* **2021**, *101*, e202000349. [[CrossRef](#)]
37. Yih, K. Uniform suction/blowing effect on forced convection about a wedge: Uniform heat flux. *Acta Mech.* **1998**, *128*, 173–181. [[CrossRef](#)]
38. Yacob, N.A.; Ishak, A.; Pop, I. Falkner–Skan problem for a static or moving wedge in nanofluids. *Int. J. Therm. Sci.* **2011**, *50*, 133–139. [[CrossRef](#)]
39. White, F.M. *Viscous Fluid Flow*, 2nd ed.; McGraw-Hill: New York, NY, USA, 1991.
40. Ali, H.; Khan, M. Impact of heat transfer analysis on Carreau fluid flow past a static/moving wedge. *Therm. Sci.* **2018**, *22*, 809–820. [[CrossRef](#)]
41. Jamshed, W.; Aziz, A. Entropy Analysis of TiO₂-Cu/EG Casson Hybrid Nanofluid via Cattaneo-Christov Heat Flux Model. *Appl. Nanosci.* **2018**, *8*, 1–14.
42. Jamshed, W.; Nisar, K.S. Computational single phase comparative study of Williamson nanofluid in parabolic trough solar collector via Keller box method. *Int. J. Energy Res.* **2021**, *45*, 10696–10718. [[CrossRef](#)]
43. Jamshed, W.; Devi, S.U.; Nisar, K.S. Single phase-based study of Ag-Cu/EO Williamson hybrid nanofluid flow over a stretching surface with shape factor. *Phys. Scr.* **2021**, *96*, 065202. [[CrossRef](#)]
44. Jamshed, W.; Nisar, K.S.; Ibrahim, R.W.; Shahzad, F.; Eid, M.R. Thermal expansion optimization in solar aircraft using tangent hyperbolic hybrid nanofluid: A solar thermal application. *J. Mater. Res. Technol.* **2021**, *14*, 985–1006. [[CrossRef](#)]
45. Akram, M.; Jamshed, W.; Goud, B.S.; Pasha, A.A.; Sajid, T.; Rahman, M.M.; Arshad, M.; Weera, W. Irregular heat source impact on Carreau nanofluid flowing via exponential expanding cylinder: A thermal case study. *Case Stud. Therm. Eng.* **2022**, *36*, 102190. [[CrossRef](#)]
46. Shahzad, F.; Jamshed, W.; Ahmad, A.; Safdar, R.; Alam, M.M.; Ullah, I. Efficiency evaluation of solar water-pump using nanofluids in parabolic trough solar collector: 2nd order convergent approach. *Waves Random Complex Media* **2022**, 1–37. [[CrossRef](#)]
47. Batool, S.; Rasool, G.; Alshammari, N.; Khan, I.; Kaneez, H.; Hamadneh, N. Numerical analysis of heat and mass transfer in micropolar nanofluids flow through lid driven cavity: Finite volume approach. *Case Stud. Therm. Eng.* **2022**, *37*, 102233. [[CrossRef](#)]
48. Shafiq, A.; Mebarek-OuDina, F.; Sindhu, T.N.; Rasool, G. Sensitivity analysis for Walters-B nanofluid flow over a radiative Riga surface by RSM. *Sci. Iran.* **2022**, *29*, 1236–1249.
49. Rasool, G.; Saeed, A.M.; Lare, A.I.; Abderrahmane, A.; Guedri, K.; Vaidya, H.; Marzouki, R. Darcy-Forchheimer flow of water conveying multi-walled carbon nanoparticles through a vertical cleveland Z-staggered cavity subject to entropy generation. *Micromachines* **2022**, *13*, 744. [[CrossRef](#)]
50. Rasool, G.; Shafiq, A.; Hussain, S.; Zaydan, M.; Wakif, A.; Chamkha, A.J.; Bhutta, M.S. Significance of Rosseland’s radiative process on reactive Maxwell nanofluid flows over an isothermally heated stretching sheet in the presence of Darcy–Forchheimer and Lorentz forces: Towards a new perspective on Buongiorno’s model. *Micromachines* **2022**, *13*, 368. [[CrossRef](#)]